Superpixel-Based Weighted Collaborative Sparse Regression and Reweighted Low-Rank Representation for Hyperspectral Image Unmixing

Hongjun Su, *Senior Member, IEEE*, Cailing Jia, Pan Zheng, and Qian Du, *Fellow, IEEE*

***Abstract*—Sparse unmixing with a semisupervised fashion has been applied to hyperspectral remote sensing imagery. However, the imprecise spatial contextual information, the lack of global feature and the high mutual coherences of a spectral library greatly limit the performance of sparse unmixing. In order to address these prominent problems, a new paradigm to characterize sparse hyperspectral unmixing is proposed, namely, the superpixel-based weighted collaborative sparse regression and reweighted low-rank representation unmixing (SBWCRLRU). In this method, the weighted collaborative sparse regression explores the pixels shared the same support set to help the sparsity of abundance fraction, and the reweighted low rank representation minimizes the rank of the abundance matrix to promote the spatial consistency of the image. Meanwhile, superpixel segmentation is adopted to cluster the pixels into different spatial homogeneous regions to further improve the unmixing performance. Extensive experiments results conducted on both synthetic and real data demonstrate the effectiveness of the proposed SBWCRLRU. It can not only improve the performance of hyperspectral unmixing but also outperform the existing sparse unmixing approaches.**

***Index Terms*—Hyperspectral image (HSI) unmixing, reweighted low-rank representation (LRR), simple linear iterative clustering (SLIC), weighted collaborative sparse regression.**

I. Introduction

HYPERSPECTRAL imagery (HSI) has high spectral resolution (usually less than the order of *nm*) since it can capture hundreds of narrow and adjacent spectra in the scene simultaneously. With such characteristics, HSI has been successfully applied to various aspects of earth sciences, such as image classification, target recognition, mineral exploration, and object detection [1]–[4]. However, due to the relatively low-spatial resolution of imaging spectrometers, multiple scattering during atmospheric transmission and complex distribution of surface microscopic material, mixed pixels are typically present in HSI, and each image pixel may cover several different materials. Thus, hyperspectral unmixing is an important issue for utilizing the wealth of information in hyperspectral data. The task of hyperspectral unmixing can be divided into two parts: extract the pure spectral signatures (endmembers) in the mixed pixels, and estimate their fractional proportions (abundances) [5]. The linear mixture model (LMM) assumes that the mixing between objects occurs on a macroscopic scale and that the incident solar radiation only interacts with one material. LMM has been widely applied for hyperspectral unmixing due to its computational tractability, efficiency and clear physical meaning [6]. Hence, the LMM-based spectral unmixing algorithms will be the focus of this article.

Several spectral unmixing approaches based on geometry [7]–[9], statistics [10], [11], nonnegative matrix factorization (NMF) [12]–[14], and sparse regression [5], [15] are mainly introduced in LMM. Although geometry and statistics approaches are simple and fast, the presence of pure materials assumptions in hyperspectral data are usually required and accompanied with higher computational complexity. The NMF-based methods aim to divide the hyperspectral data into two nonnegative matrices. However, it may obtain virtual endmembers with no physical meaning and lead to the defect of nonunique solution. In addition, nonlinearity and spectral variability still hinder the aforementioned LMM from producing high performance unmixing capabilities [16]. To circumvent these obstacles according to compressed sensing theory [17], [18], sparse regression-based unmixing has been successfully proposed as a new semisupervised technique. The model suggests that mixed pixels can be approximately represented by linear combinations of several pure spectral materials from a spectral library [15]. More specifically, it can effectively circumvent the negative impact about the availability of pure spectral signatures and the estimation of the number of endmembers in HSI by using a spectral library as prior knowledge. Due to the abovementioned advantages, sparse unmixing has become a hot topic.

It is difficult to obtain accurate unmixing results by traditional sparse regression unmixing model. The typical method is the sparse unmixing algorithm via variable splitting and augmented Lagrangian (SUnSAL) [19], which obtains the unmixing results by constructing a prior from the spectral library and uses the ℓ_1 norm on abundance matrix. To alleviate the high mutual coherences of atoms in the library, and the constrained version

Manuscript received September 12, 2021; revised November 12, 2021; accepted November 29, 2021. Date of publication December 7, 2021; date of current version December 30, 2021. This work was supported by the National Natural Science Foundation of China under Grant 42122008 and Grant 41871220. *(Corresponding author: Hongjun Su.)*

Hongjun Su, Cailing Jia, and Pan Zheng are with the School of Earth Sciences and Engineering, Hohai University, Nanjing 211100, China (e-mail: hjsu@hhu.edu.cn; cljia95@163.com; zhengpan1013@163.com).

Qian Du is with the Department of Electrical and Computer Engineering, Mississippi State University, Starkville, MS 39762 USA (e-mail: du@ece.msstate.edu).

Digital Object Identifier 10.1109/JSTARS.2021.3133428

of the same algorithm called collaborative SUnSAL (CLSUnSAL) was introduced in [20]. CLSUnSAL used $\ell_{2,1}$ norm to constrain the row sparsity of abundance matrix. Furthermore, in [21]–[23], the strategies of iteratively weighted sparsity also obtained satisfactory results. However, these algorithms only interpret the sparsity of abundance coefficients and the availability of spectral information, but spatial contextual information is generally ignored, which may provide limited unmixing performance and high computational complexity, especially for observed HSI degraded by noise.

On the other hand, the methods based on spatial prior information are exploited in many works [23]–[25]. Its basic idea is to introduce spatial prior information into the sparse regression framework to constrain optimization problem. The total variation (TV) regularization for sparse unmixing (SUnSAL-TV) [24] strictly defines that a pixel is only similar to its four neighboring pixels, which have similar fractional abundance. A spectral spatial weighted sparse unmixing (S^2WSU) [23] method is proposed to investigate spectral and spatial information simultaneously, and it uses both spectral and spatial weighted factors, one of which is used to promote nonzero row vectors, and the other is used to utilize the spatial correlation information. From a different perspective, the nonlocal total variation (NLTV) prior is used to the NMF model [25], the nonlocal similarity is clarified, and smoothness of the entire image and the spatial diversity distribution of endmembers are described. The sparse unmixing methods with spatial information have shown a great potential, but adopting regular-shaped neighborhoods to explore the correlation between pixels limits the accurate description of the spatial-contextual information around each pixel of the image [26]–[28]. Thus, superpixel segmentation is used to combine global spatial neighborhood information and spectral information, and it provides a good solution to the aforementioned issues. Each superpixel can be regarded as a small nonoverlapping spatial region, and its shape and size can be adaptively changed [29]. Typically, a fast sparse multiscale sparse unmixing algorithm (MUA) is proposed [30], where spectral unmixing is first performed in the approximate domain images by using superpixel segmentation method, and then, the coarse domain unmixing results are used to guide the original domain unmixing to obtain more meaningful spatial information. Yang *et al*. [31] developed a hyperspectral unmixing method based on superpixel segmentation, and nonlocal spatial information is combined with spatial group sparsity effectively. A superpixel-based technique to guide the sparse unmixing is also adopted by Zhang *et al*. [32]. Readers can also refer to the literature, such as [33]–[35], to comprehend the semisupervised hyperspectral unmixing methods based on superpixel segmentation.

Recently, low-rank representation (LRR) has received considerable attention for better learning the spatial-spectral low-dimensional embedding [14], [36]. The joint sparse and low-rank learning [37] method is introduced for spectral unmixing by sharing sparse coefficients and performing low-rank constraints. To simultaneously take advantage of sparsity and correlation, alternating direction sparse and low-rank unmixing [38] is performed with weighted nuclear norm in a small area of the abundance matrix determined by the regular sliding windows. In [39], joint sparse blocks and low-rank unmixing method is employed to achieve low-rank approximation of abundance coefficients by using the global abundance weighted nuclear norm. Furthermore, superpixel-based reweighted low-rank and TV (SUSRLR-TV) is purported by Li *et al*. [40], where the rank of the abundance matrix is minimized after superpixel segmentation, and the visual smoothness of the abundance maps is encouraged by using TV. However, a large nonsmooth convex optimization problem and unacceptable time complexity will incur when compared with the expected hyperspectral unmixing images.

In summary, the existing hyperspectral sparse unmixing methods combined with spatial information mostly ignore the spectral similarity and location proximity of local pixels. In this article, a new approach of sparse spectral unmixing algorithm *based on superpixel weighted collaborative sparse regression and reweighted low rank representation for hyperspectral image unmixing* (SBWCRLRU) is proposed, and both spectral correlative and spatial low-rank characteristics of each superpixel in HSI are considered in this method. Specially, the simple linear iterative clustering (SLIC) segmentation is integrated into abundance matrix for reducing the solution space. The main contributions of SBWCRLRU algorithm in this article can be summarized as follows.

1) Superpixel segmentation is considered in spectral unmixing, where spatial and spectral features can be extracted from more meaningful regions rather than from a square local patch. Since the size of superpixels is significantly smaller than the original image, unmixing within each superpixel can greatly reduce computational burden.
2) For better promoting the sparsity and overcome the shortcomings of the original collaborative sparse unmixing method, a collaborative sparse constraint is imposed on each superpixel. In addition, a spatial weighting factor is introduced to enhance the reconstruction of abundance maps.
3) To overcome the problem of edge blur caused by the TV regularization term, a new reweighted LRR is added to minimize the rank of the abundance vector in each superpixel. Experimental results show that the constraint can maintain the internal local low-dimensional spatial structure of the image.

The rest of this article is organized as follows. In Section II, a detailed explanation of sparse unmixing is presented. Section III is dedicated to introduce the proposed SBWCRLRU and the alternating direction methods of multipliers (ADMM) algorithm to address the minimization problem. Section IV presented experiment results on two simulated data and three real hyperspectral datasets with different algorithms. Section V discussed the parameters selection of our method. Finally, Section VI concludes this article.

II. Related Work

A. Sparse Unmixing Model Based on LMM

The LMM model assumes that the spectra collected by the imaging spectrometer in the real scene can be approximately

expressed as a linear operation of some spectral signatures from the library [5], [6], [15]. Hence, an HSI can be expressed in matrix form as

$$Y = DX + E \tag{1}$$

where $Y \in R^{L\times n}$ denotes the observed vector with L spectral bands and n pixels, $D \in R^{L\times m}$ is a large spectral library with m spectral signatures, $X \in R^{m\times n}$ refers to the abundance vector of all endmembers in each pixel that is compatible with spectral library D, and $E \in R^{L\times n}$ is an observation noise or the model error vector.

Generally, abundance estimation can be expressed as an inverse problem. To conform the physical limitation of hyperspectral sparse unmixing model, there are two important constraints of abundance matrix are imposed, which are the *abundance nonnegativity constraint* (*ANC*) and *a sum to one constraint* (*ASC*) [15]

$$\begin{aligned} &ANC: X \geq 0 \\ &ASC: 1^T X = 1^T. \end{aligned} \tag{2}$$

The ASC is not always satisfied due to the random selection of endmembers from the spectral library (which does not necessarily cover all the endmembers in HSI) and the strong spectral variability in the real scene. Thus, the ASC is not delved into sparse unmixing model in this article [15].

In practice, since the number of spectral signatures in the available spectral library D is much larger than the real-hyperspectral scene, that is, the abundance coefficient vector of each pixel has only a few nonzero elements, and the abundance matrix X manifests sparse characteristics. Therefore, the sparse unmixing model can be written as

$$\arg\min_X \frac{1}{2}\|DX - Y\|_F^2 + \lambda\|X\|_0 + \ell_{R_+}(X) \tag{3}$$

where $\|\cdot\|_F = \sqrt{trace\{XX^T\}}$ represents the Frobenius norm of the abundance matrix X, and $\lambda > 0$ is a regularization parameter, which is controlling the balance between the data fidelity term and the sparse constraint term. Here, $\|X\|_0$ denotes the number of nonzero components in the abundance matrix X, that is, ℓ_0 norm. $\ell_{R_+}(X) = \sum_{i=1}^n \ell_{R_+}(x_i)$ is the indicator function, which represents the nonnegative constraint of $X \geq 0$. For $x_i > 0, \ell_{R_+}(x_i) = 0$, and otherwise, $\ell_{R_+}(x_i) = \infty$

Although the ℓ_0 norm can describe the sparsity of abundance coefficients well, the solution of (3) is NP-hard and difficult to solve [41], [42]. Generally, a nonconvex ℓ_0 norm can be replaced by a convex ℓ_ρ norm [43] under certain assumptions [41], [44], and both have the same optimal solution. Then, the optimization problem is expressed as

$$\arg\min_X \frac{1}{2}\|DX - Y\|_F^2 + \lambda\|X\|_{\rho,1} + \ell_{R_+}(X). \tag{4}$$

When setting $\rho = 1$, (4) is reduced to the typical SUnSAL sparse unmixing model [19], where $\|X\|_{1,1} = \sum_{j=1}^n \|x^j\|_1$ and presents the j th column of abundance matrix X. However, the ℓ_0 norm does not adequately characterize the sparsity of the spectral signatures, which affects the accuracy of hyperspectral unmixing to a certain extent.

Considering the general situation, the observed vector requires only a few spectra of the library to participate in the unmixing, then the abundance matrix corresponding to the observed vector is a row sparse matrix. Thus, setting $\rho = 2$, (4) is actually the CLSUnSAL sparse unmixing model [20], where $\|X\|_{2,1} = \sum_{i=1}^m \|x^i\|_2$ is the $\ell_{2,1}$ mixed norm. Here, x^i is the i th row of X. Obviously, the row sparsity constraint makes most of the row vectors in the abundance matrix X zero, which improves the accuracy of unmixing.

III. Proposed Method

A. HSI Representation Using Superpixel Segmentation

The spatial structure cannot be accurately described in traditional hyperspectral unmixing due to the spatial resolution of HSI and adjacent pixels are likely to be from the same class in the scene. Consequently, how to accurately capture the characteristics of actual hyperspectral data and effectively utilize spectral-spatial information is one of the main research contents of this article. At present, superpixel segmentation [29], [45] provides an effective solution for this purpose. Superpixel segmentation divides the HSI into perceptually disconnected homogeneous regions with similar properties, each of which is called a superpixel. The value of superpixel segmentation in the unmixing processing of HSI has been recognized in the literature [30], [34], [35], [40]. Thus, the obtained homogeneous and uniform regions-based superpixel segmentation method is adopted in this article. In particular, SLIC [46] algorithm is simple, and computationally efficient, and generates superpixels that are uniformly sized and irregularly shaped, which is more in line with the expected segmentation effect. The proposed hyperspectral SLIC is iterative.

SLIC first divided the HSI into equally spaced grids based on a predefined number of superpixels, as shown in Fig. 1(b). Then, the center of each grid is evenly distributed in the image and initialized with spatial adjacency constraints. Assuming that the image with N pixels, is predivided into K equally spaced grid and the size of each grid is N/K, then the distance between the center points (seed points) of adjacent grids can be defined as $S = \sqrt{N/K}$. It is worth noting that SLIC algorithm needs to be adapted to hyperspectral problems, where a clustering center is the vector connecting spectral information and spatial coordinates rather than the original RGB distance [29], [33], [47]. For pixels i and j, the distance is calculated as

$$d_1 = (y_i - y_j)_2 \tag{5}$$

$$d_2 = \sqrt{(a_i - a_j)^2 + (b_i - b_j)^2} \tag{6}$$

$$D(i,j) = \sqrt{\alpha d_1^2 + d_2^2} \tag{7}$$

where y_i and y_j represent the spectral vectors of pixels i and j , respectively, and $D(i,j)$ denotes the dissimilarity between pixels i and j, calculated by combining the spectral distance d_1 and spatial distance d_2. In addition, α is the weighted between d_1 and d_2, which in general is a constant.

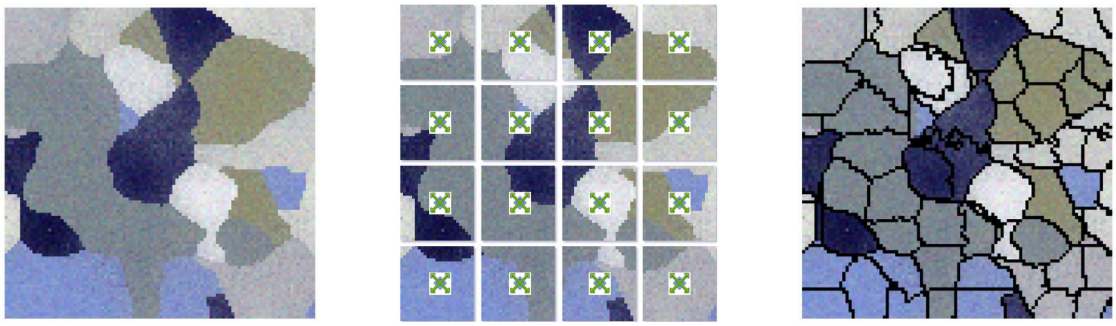

(a) (b) (c)

Fig. 1. SLIC segmentation for hyperspectral data. (a) Original image. (b) Initialization stage. (c) Final segmentation.

After clustering, any fragments with area less than a predefined threshold are selectively deleted at each iteration process, and then the surrounding pixels of the seeds are merged into a larger superpixel. Each seed point is moved in a (3×3) neighborhood until the gradient of the corresponding position is the lowest, so as to prevent seed points from being located on the boundary of the image and affect the overall effect of clustering [33], [48], [49].

Finally, class labels are assigned to all pixels contained in each merged superpixel. At the end of each round of labeling, the abovementioned steps are repeated with the average value of the same class of pixels as the new seed point, and iteration until convergence. The final result of a segmentation is shown in Fig. 1(c).

The constraints to the abundance maps in each superpixel are added to shrink the solution space. Generally, two kinds of priors are analyzed in constraining the abundance matrix of each superpixel, that is, weighted collaborative sparse regression prior and reweighted LRR prior, which are introduced in the following two sections.

B. Weighted Collaborative Sparse Regression Prior

Since each superpixel is a subimage of HSI, the sparsity of superpixel is an important manifestation of the sparsity of HSI. In the actual unmixing process, only some of the spectral signatures of the library participate in the unmixing of the hyperspectral data. Thus, the abundance matrix of each superpixel reflects the characteristics of row sparsity of sparsity, which means that only a few rows in the abundance matrix of each superpixel are nonzero, and the row sparsity is stronger than ℓ_1 norm. Hence $\ell_{2,1}$ mixed norm is adopted instead of ℓ_1 norm. Inspired by [23], [50], and [51], sparse unmixing is performed while considering the additional constraint provided by weighting to enhance the sparsity of abundance vector in the spectral domains. The following weighted sparse regression formulation for unmixing of superpixels is represented:

$$\arg\min_{X} \frac{1}{2} \|DX - Y\|_F^2 + \lambda \sum_{k=1}^{S} \|X_k\|_{w_k 2,1} + \ell_{R_+}(X). \quad (8)$$

The term $\|X_k\|_{w_k,2,1} = \sum_{i=1}^{m} w_{i,k} \|X_k^{[i]}\|_2$ is the weighted $\ell_{2,1}$ mixed norm to promote joint sparsity among all the pixels and improve the unmixing accuracy in each superpixel. Here, $X_k^{[i]}$ denotes the i th row of the k th superpixels of abundance matrix X, for $i = 1, \ldots, m$, $k = 1, \ldots, S$, and $w_k = [w_{1,k}, \ldots, w_{m,k}]^T$ is a nonnegative weight vector to promote row sparsity mainly.

C. Reweighted LRR Prior

To the best of our knowledge, an interesting relationship exists between the sparsity and low-rank properties, and the abundance matrix also demonstrates the characteristics of low-rank, because the neighborhood pixels of HSI are usually composed of the same endmembers with similar abundance proportion. In order to capture this data structure with low-rank and sparse nature, a low-rank constraint of the abundance matrix has been imposed on sparse unmixing [52], [53]. A new weighting strategy under the low-rank unmixing framework is developed, that is, each row in superpixels is assigned a different weighting coefficient at each iteration to promote the image to maintain a low-rank structure. Therefore, a sparse LRR optimization problem for unmixing can be expressed as

$$\arg\min_{X} \frac{1}{2} \|DX - Y\|_F^2 + \lambda \sum_{k=1}^{S} \|X_k\|_{w_k,2,1} + \tau \sum_{k=1}^{S} \sum_{j=1}^{R} \|X_k\|_{\omega,*} + \ell_{R_+}(X) \quad (9)$$

where the term $\|X_k\|_{\omega,*} = \sum_{i=1}^{\operatorname{rank}(X_k^{[j]})} \omega_i \sigma_i(X_k^{[j]})$ is the weighted nuclear norm to realize singular value shrinkage by assigning different weights to each singular value. $\omega_i, i = 1, \ldots, r$ denotes the nonnegative weights and σ_i is the singular value of a matrix $X_k^{[j]}$, $X_k^{[j]} = [X_k^{[1]}, \ldots, X_k^{[R]}]^T$ denotes the j th submatrix of k th superpixels of X, and R represents the number of submatrices in each superpixel. Here, τ is nonnegative regularization parameter that controls the importance of low-rank of the related terms. The nuclear norm provides an estimate of the low-rank approximation of abundance matrix and can be easily solved by the singular value threshold (SVT) method.

Algorithm 1: Pseudocode of Proposed **SBWCRLRU**.

Input: $Y, D, \lambda, \tau, \mu, \varepsilon,$ the number of superpixels Φ
Initialization: set $t = 0, k = 0, P_1^{(0)}, P_2^{(0)}, P_3^{(0)}, P_4^{(0)}, M_1^{(0)}, M_2^{(0)}, M_3^{(0)}, M_4^{(0)}$
Repeat:
for $g = 1to\Phi$
Compute $W_{S_g}^{(k)}$ using (10)
end for
Repeat:
$Q^{(t+1)} \leftarrow (D^T D + 3I)^{-1}(D^T(P_1^{(t)} + M_1^{(t)}) + (P_2^{(t)} + M_2^{(t)}) + (P_3^{(t)} + M_3^{(t)}) + (P_4^{(t)} + M_4^{(t)}))$
$P_1^{(t+1)} \leftarrow \frac{1}{1+\mu}(Y + \mu(DQ^{(t+1)} - M_1^{(t)}))$
for $g = 1to\Phi$
$P_{2_g}^{(t+1)} \leftarrow \text{vect\_soft}(Q_g^{(t+1)} - M_{2_g}^{(t)}, \frac{\lambda}{\mu} W_{S_g}^{(k)})$
$P_{3_g}^{(t+1)} \leftarrow T_{\omega, \frac{\tau}{\mu}}(Q_g^{(t+1)} - M_{3_g}^{(t)})$
end for
$P_4^{(t+1)} \leftarrow \max(Q^{(t+1)} - M_4^{(t)}, 0)$
Update Lagrange multiplier:
$M_1^{(t+1)} \leftarrow M_1^{(t)} - DQ^{(t+1)} + M_1^{(t+1)}$
$M_i^{(t+1)} \leftarrow M_i^{(t)} - Q^{(t+1)} + M_i^{(t+1)} (i = 2, 3, 4)$
Update inner loops iteration: $t \leftarrow t + 1$
$Q^{(k+1)} \leftarrow Q^{(t+1)}$
$M_2^{(k+1)} \leftarrow M_2^{(t+1)}$
Update outer loops iteration: $k \leftarrow k + 1$.
Until stopping criterion is fulfilled.

D. Selection of Weighting Coefficients

To promote the sparsity of rows and singular values of each superpixel, the selection of weighting coefficients of $w_{i,k}$ values in (8) and ω_i in (9) are interpretated in this part. For simplicity, let a represent sparse weighting factor $w_{i,k}$ and b represent low-rank weighting factor ω_i.

Exploring the importance of spatial information and relying on success of [23] and [36] the spatial weighting factor into the unmixing model is integrated to maintain the consistency and uniformity of abundance matrix. Therefore, the weighting factor can be described as

$$a^{(t+1)} = \frac{1}{f_{h \in \mathcal{M}(j)}(x_{ih}^{(t)}) + \delta} \tag{10}$$

where $f(x_{ij}) = (\sum_{h \in M(j)} \in_{ih} x_{ih})/(\sum_{h \in M(j)} \in_{ih})$, which captures the spatial correlations in each superpixel through the neighborhood domain $\mathcal{M}(j)$, and δ is a small positive constant (this article sets it to 1e–6). For simplicity, the neighboring coverage identified here is 8-connected (3×3 window) for experiments and Euclidean distance is defined, that is, $\in_{ij} = (1/((c-q)^2 + (d-z)^2)^{1/2})$ represents the neighborhood importance for $x_i(c, d)$ and $x_j(q, z)$.

Similarly, inspired by [36] and [53], minimizing the rank of the abundance matrix in each superpixel to protect the main features and ignore the unimportant or noisy parts in HSI, the weighting coefficient b for weighted nuclear norm is selected, that is

$$b^{(t+1)} = \frac{1}{\sigma_i^{(t)} + \varepsilon} \tag{11}$$

where σ_i is the singular value and ε is a preset positive constant to prevent the denominator from being zero meaningless. Clearly, the singular value of the abundance matrix of each superpixel is relatively large, indicating that the singular value is the principal component of the abundance matrix. Hence, a large weight is used to attenuate nonzero singular values and a small weight is used to encourage nonzero singular values in the unmixing processing of HSI [39], [54], [55], the smaller singular values should be attenuated as much as possible and the larger singular values should be attenuated as little as possible.

Under the ADMM [56] framework, SBWCRLRU is summarized in Algorithm 1. It should be noted that the convergence of Algorithm 1 is difficult to justify. The inner and outer loop iterative method is adopted to solve the optimization problem of the model [23], [34]. The inner loop corresponds to the update of the abundance coefficients via the ADMM and the outer loop corresponds to the update of the spatial weight. More details can be found in the Appendix.

IV. Experiments

To evaluate the performance of the proposed SBWCRLRU method, two simulated datasets and three real remotely sensed image are used in the comparison with SUnSAL-TV, S^2WSU, MUA_{SLIC}, SUSRLR-TV, and SUnCNN [57].

A. Simulated Data Experiments

1) *Data description:* Two simulated hyperspectral datasets are adopted in our experiments, i.e., SD1 and SD2. Both use the same spectral library $D \in R^{224 \times 240}$, which is generated by randomly selecting 240 different materials from the U.S. Geological Survey (USGS) library[1] consisted of 224 spectral signatures in $0.4 - 2.5\,\mu$m [5], [15]. Their fractional abundances are subject to the *ANC* and *ASC* constraints. The first dataset (SD1) consists of 224 bands of 75×75 pixels formed by five randomly selected signatures from the spectral library D as endmembers. With abundance generated by [24], and spatially distributed in the form of a square area, the background mixture is composed of five endmembers with fractional abundances 0.1149, 0.0742, 0.2003, 0.2055, and 0.4051. In the second dataset (SD2), nine spectral signatures from the spectral library D are selected randomly as active endmembers, and the corresponding fractional abundance maps with the spatial size of 100×100 pixels are adopted, which were sampled according to a Dirichlet distribution centered on the Gaussian random field [34]. These two simulated data are contaminated by the Gaussian noise of the signal-to-noise ratio (SNR), i.e., 20, 30, and 40 dB.

2) *Visual quality comparison:* For the simulated datasets, Figs. 2 and 3, respectively, show the true and estimated abundance maps through different unmixing algorithm with $SNR = 30$ dB. It can be observed that the SUnSAL-TV adds

[1][Online]. Available: http://speclab.cr.usgs.gov/spectral.lib06

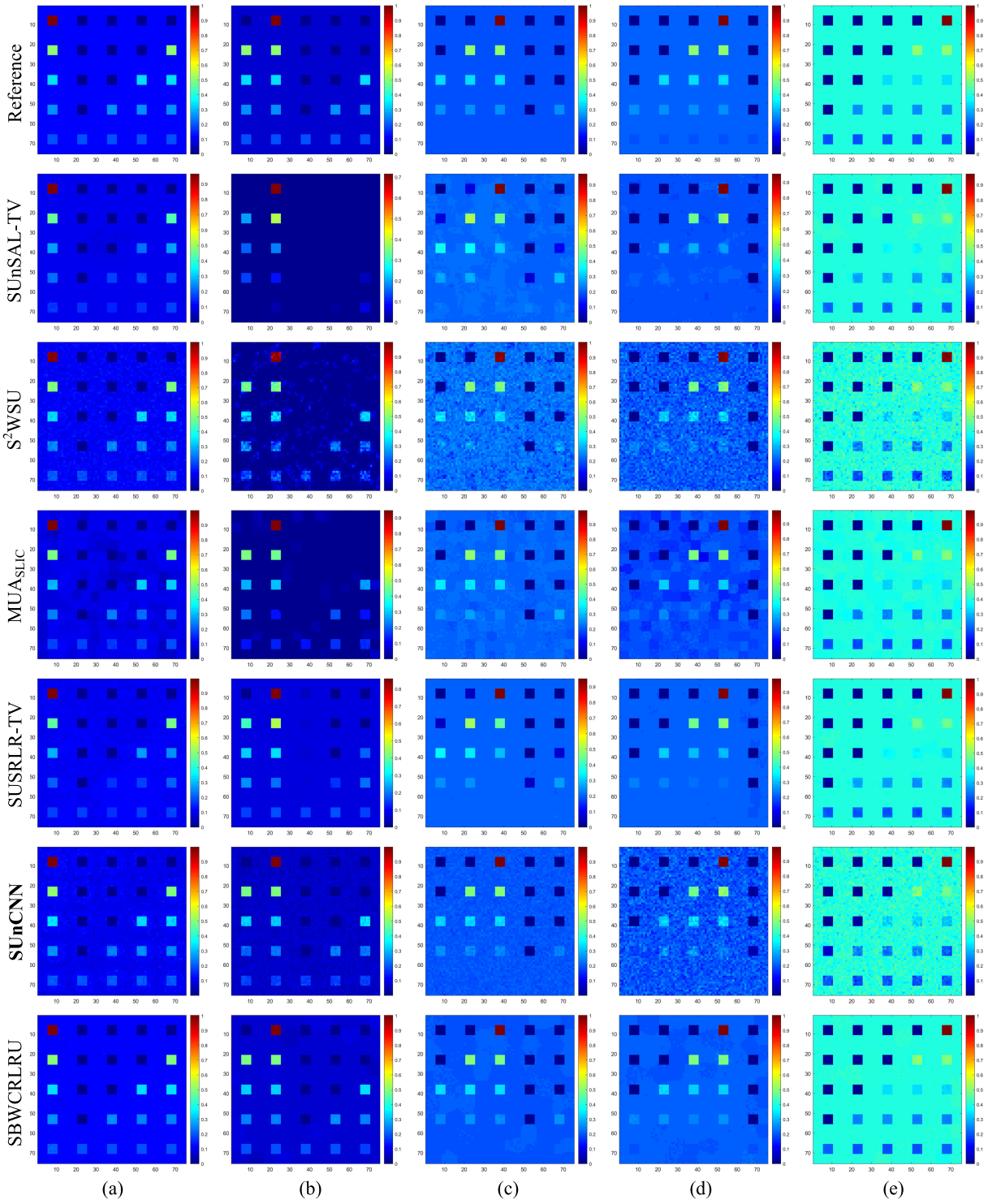

Fig. 2. SD1 with SNR = 30 dB results: abundance maps estimated by different methods. (a) Endmembers #1. (b) Endmember #2. (c) Endmember #3. (d) Endmember #4. (e) Endmember #5.

the spatial information and provides relatively good unmixing effect. However, for endmember #5 of the SD1 and endmember #2 of the SD2, the boundary of square region and the contour of the abundance maps can be clearly described, which obviously leads to excessive smoothness and blurring phenomenon. Moreover, there contains many noisy points after using S^2WSU, because the spatial relationship in the local windows is only dissected, and the spatial penalty constrains is not sufficient. Although the $\mathrm{MUA}_{\mathrm{SLIC}}$ algorithm could express the spatial information of the unmixed target well, there still exist some artifacts areas, which cannot be distinguished well. Part of the abundance maps seems to be light-colored by using the

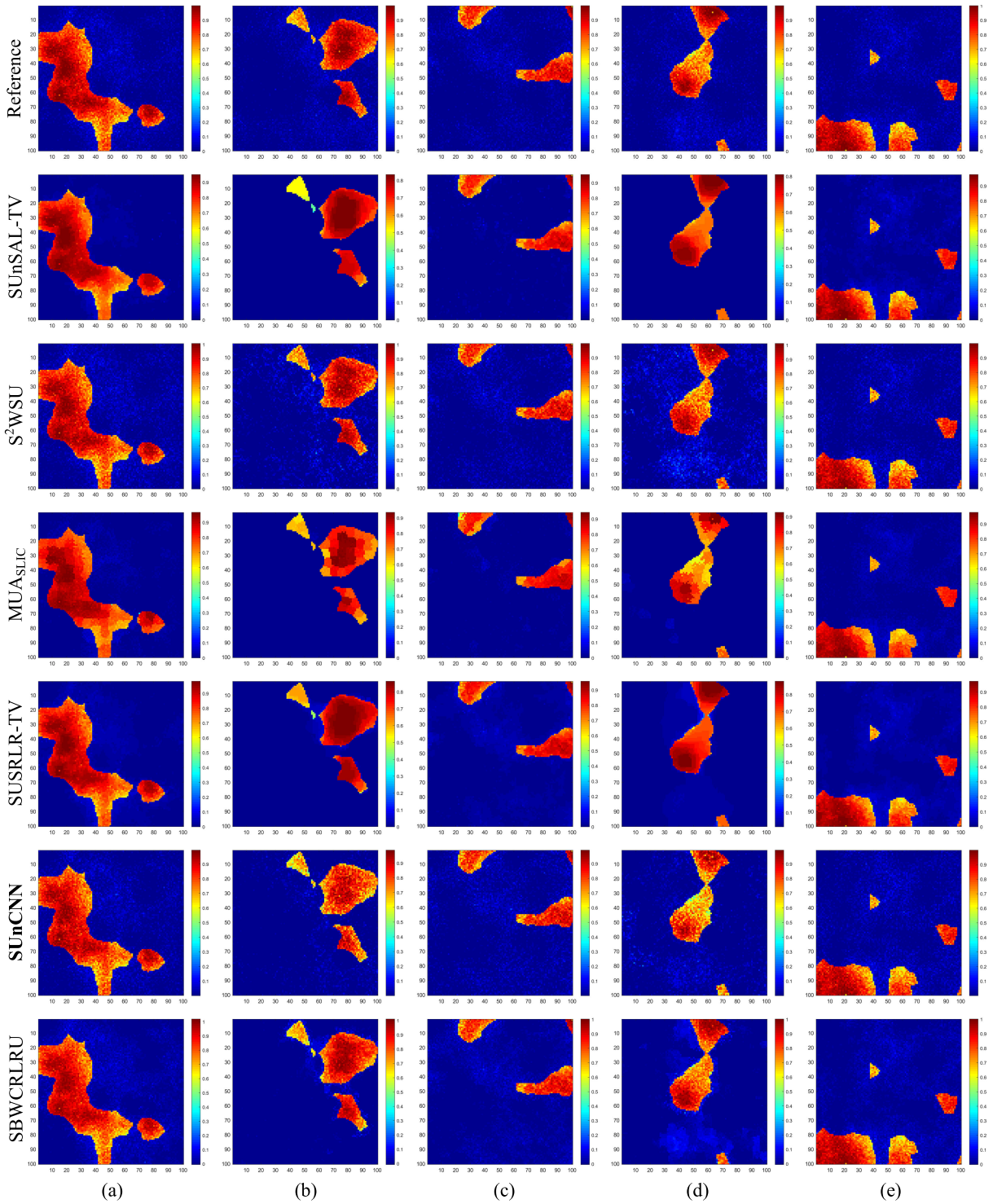

Fig. 3. SD2 with SNR = 30 dB results: abundance maps estimated by different methods. (a) Endmember #1. (b) Endmember #2. (c) Endmember #4. (d) Endmember #7. (e) Endmember #9.

SUSRLR-TV algorithm, such as the upper right corner of SD1 endmember #2, and misidentification was observed in the small areas of SD2 endmember #7, and the error caused the real abundance maps to be distorted. For the SUnCNN method combined with deep learning, it can better preserve the texture information of the HSI due to the convolutional operator, but it contains much noisy points in SD1 endmember #4 that do not conform to the actual. In the proposed SBWCRLRU, all the experimental results in SD1 and SD2 datasets generate abundance maps with better spatial consistency than other approaches, and the results are similar to the ground-truth abundance maps, which can effectively circumvent the problem of edge blurring, and reveal a good compromise between smoothing the boundary and keeping details.

TABLE I
SRE AND RMSE VALUES OF DIFFERENT UNMIXING ALGORITHMS ON THE SD 1 (THE OPTIMAL PARAMETERS ARE INDICATE)

SNR	Criteria	**SUnSAL-TV**	**S²WSU**	**MUA$_{SLIC}$**	**SUSRLR-TV**	**SUnCNN**	**SBWCRLRU**
40dB	SRE	17.47	28.23	22.38	37.65	30.7948	**44.59**
	RMSE	0.0046	0.0013	0.0023	0.0005	0.0010	**0.0002**
		$\lambda = 5e-3$ $\lambda_{TV} = 1e-3$	$\lambda = 1e-3$	$\lambda_1 = 1e-3$ $\lambda_2 = 1e-2$	$\rho = 1e-2$ $\lambda_{TV} = 5e-4$	$Iter = 12000$	$\tau = 5e-2$ $\lambda = 1e-4$
30dB	SRE	14.43	15.49	15.73	24.59	20.8620	**34.66**
	RMSE	0.0066	0.0058	0.0056	0.0020	0.0031	**0.0006**
		$\lambda = 7e-3$ $\lambda_{TV} = 1e-2$	$\lambda = 5e-3$	$\lambda_1 = 7e-3$ $\lambda_2 = 5e-2$	$\rho = 5e-2$ $\lambda_{TV} = 1e-2$	$Iter = 8000$	$\tau = 1e-1$ $\lambda = 5e-4$
20dB	SRE	9.53	7.70	11.35	13.31	10.8071	**20.24**
	RMSE	0.0115	0.0142	0.0094	0.0075	0.0100	**0.0034**
		$\lambda = 5e-2$ $\lambda_{TV} = 5e-2$	$\lambda = 1e-1$	$\lambda_1 = 3e-2$ $\lambda_2 = 1e-1$	$\rho = 1e-1$ $\lambda_{TV} = 5e-2$	$Iter = 4000$	$\tau = 8e-1$ $\lambda = 5e-3$

TABLE II
SRE AND RMSE VALUES OF DIFFERENT UNMIXING ALGORITHMS ON THE SD 2 (THE OPTIMAL PARAMETERS ARE INDICATED)

SNR	Criteria	**SUnSAL-TV**	**S²WSU**	**MUA$_{SLIC}$**	**SUSRLR-TV**	**SUnCNN**	**SBWCRLRU**
40dB	SRE	20.62	24.88	20.19	25.81	**29.2855**	27.11
	RMSE	0.0051	0.0031	0.0053	0.0028	**0.0019**	0.0024
		$\lambda = 5e-3$ $\lambda_{TV} = 1e-3$	$\lambda = 5e-3$	λ_1=1e-3 λ_2=1e-2	$\rho = 1e-2$ $\lambda_{TV} = 1e-3$	$Iter = 12000$	$\tau = 5e-3$ $\lambda = 5e-5$
30dB	SRE	18.03	21.54	18.13	21.16	21.3798	**22.25**
	RMSE	0.0068	0.0046	0.0068	0.0048	0.0047	**0.0042**
		$\lambda = 5e-3$ $\lambda_{TV} = 7e-3$	$\lambda = 5e-3$	$\lambda_1 = 7e-3$ $\lambda_2 = 5e-2$	$\rho = 5e-2$ $\lambda_{TV} = 1e-2$	$Iter = 8000$	$\tau = 3e-2$ $\lambda = 5e-4$
20dB	SRE	11.86	9.33	14.82	15.24	13.0551	**15.53**
	RMSE	0.0139	0.0186	0.0099	0.0094	0.0121	**0.0091**
		$\lambda = 1e-2$ $\lambda_{TV} = 3e-2$	$\lambda = 1e-2$	$\lambda_1 = 7e-3$ $\lambda_2 = 1e-1$	$\rho = 5e-2$ $\lambda_{TV} = 3e-2$	$Iter = 4000$	$\tau = 1e-1$ $\lambda = 1e-2$

3) *Quantitative comparison:* To further quantitatively evaluate the performance of the proposed SBWCRLRU on the simulated datasets SD1 and SD2, the three image quality evaluation indicators are applied to measure the error between the reconstructed abundance maps $\widehat{Y}$ and the original image Y. Here, the L represents the number of spectral bands of observed vector, and N represents the number of pixels in each band of observed vector. For convenience, the $\hat{Y}$ and Y are converted into corresponding 2-D matrix to calculate these indicators.

SRE (dB) is defined as signal to reconstruction error in the following equation, which represents the ratio between the reconstructed abundance matrix and the true abundance matrix. The higher the SRE, the higher quality of the unmixing results.

$$SRE(Y,\hat{Y}) = 10\log_{10}\left(\frac{E\left[\|Y\|_2^2\right]}{E\left[\left\|Y-\hat{Y}\right\|_2^2\right]}\right). \tag{12}$$

RMSE is root mean square error defined in the following equation, which is to measure the quality of the image to be tested from a global perspective by calculating the difference between the corresponding pixels of the two images. The smaller the value, the better.

$$RMSE(Y,\hat{Y}) = \sqrt{\frac{1}{LN}\left\|Y-\hat{Y}\right\|_F^2}. \tag{13}$$

PSNR is peak SNR defined in the following equation, which is a common and widely used metric to evaluate the image quality. The difference between the corresponding pixels of the real image and the estimated image is regarded as the criterion for judging the image quality, where MSE stands for the mean square error, the larger the PSNR value, the smaller the image distortion and the better the quality.

$$\mathrm{PSNR}(Y,\hat{Y}) = 10\log_{10}\left(\frac{\max(Y)^2}{\mathrm{MSE}(Y,\hat{Y})}\right) \tag{14}$$

Tables I and II list the SRE (dB) values and the RMSE values of all comparison algorithms for SD1 and SD2 with optimal regularization parameters values, the best results of each algorithm are bolded. First, the longitudinal comparison of the different SNR in the tables shows that the difference between different algorithms will be significantly amplified with the reduction of noise level, especially, the performance of S²WSU decreases significantly when the SNR is reduced. Second, the horizontal comparison of the different algorithms shows that the sparse unmixing methods incorporating spatial contextual information and displays great potential in unmixing performance, which is obviously better than the traditional sparse unmixing algorithm. Finally, the SBWCRLRU method illustrates good results on the evaluation indexes of SRE and RMSE, which are consistent with the visual results in Figs. 2 and 3, as well as our expectations. The improvement of SD1 at 20, 30, and 40 dB is particularly significantd because the change of SRE is at least greater than 8 dB. It further reveals that the weighted collaborative sparse regression and reweighted LRR method can not only enhance the

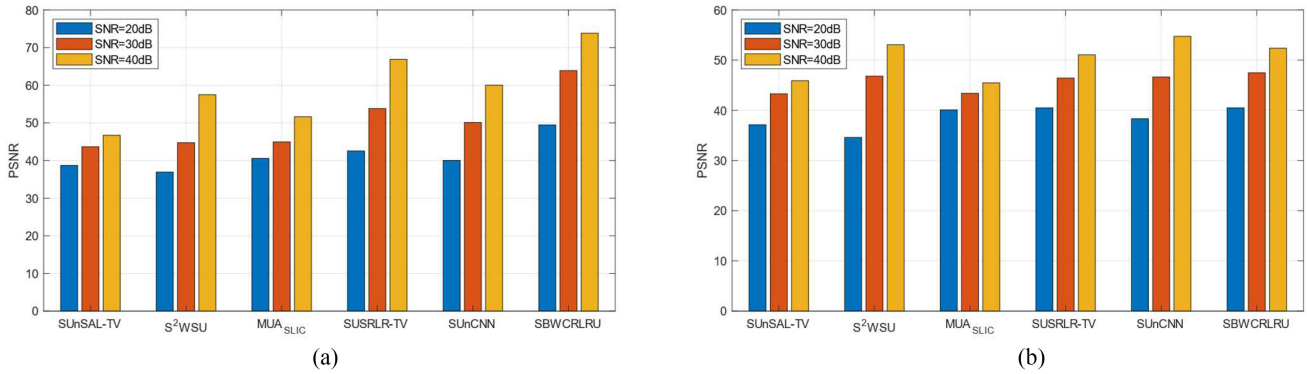

Fig. 4. Difference of each algorithm in PSNR evaluation indicator for simulated datasets. (a) SD1. (b) SD2.

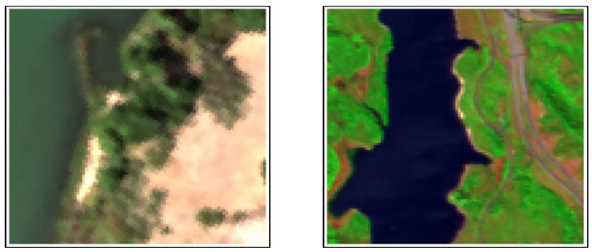

Fig. 5. Pseudocolor images of the test datasets. (a) Samson. (b) Jasper Ridge.

sparsity of the solution of the abundance matrix, but also improve the consistency of the spatial information of the abundance graph, so as to improve the accuracy of unmixing.

In order to obtain the difference of each algorithm in PSNR evaluation indicator, the bar chart is shown in Fig. 4. It can be seen that the SBWCRLRU algorithm has considerable unmixing results on the simulated datasets compared with other methods.

B. Real Hyperspectral Data Experiments

1) *Samson data*: The data are generated by the SAMSON sensor [14]. It contains 156 channels with the wavelengths from 0.401∼0.889 μm. For the sake of simplicity, a subset composed of 95 × 95 pixels is utilized in this experiment. Soil, trees, and water are selected as references for the three endmembers.
2) *Jasper Ridge data*: The data are captured by the AVIRIS sensor [13]. Jasper Ridge data has been widely used in performance testing of hyperspectral unmixing. It contains 224 bands with a spectral resolution of 9.46 nm. Moreover, to avoid atmospheric influence, some unusable frequency bands are deleted (198 channels are reserved). It has 100 × 100 pixels and 198 spectral bands for experimentation, and four endmembers are assumed to exist in Jasper Ridge dataset: tree, water, soil, and road. The pseudocolor images of Samson and Jasper Ridge datasets are shown in Fig. 5.
3) *Cuprite data*: Cuprite dataset measured by AVIRIS sensor, is composed of 250×191 pixels. The Cuprite data contain 224 bands, covering the 0.4∼2.5 μm wavelength. As an experiment, removing the low SNR and atmospheric absorption bands, and the 188 effective bands are remained. The portion subset of the Cuprite dataset (enclosed by the red rectangle, as shown in Fig. 6) is used in our experiment. Since the true abundance maps of this HSI is not available [24], the three main minerals abundance maps in Cuprite district are compared, namely Alunite, Buddingtone, and Chalcedony. The parameters of all algorithms were selected empirically, specifically, the regularization parameters of the algorithms under comparison are set as $\lambda = 1e-3$ and $\lambda_{\mathrm{TV}} = 1e-3$ for SUnSAL-TV, $\lambda = 0.07e-3$ for S^{2}WSU, $\lambda_1 = 1e-3$ and $\lambda_2 = 1e-3$ for MUA$_{\mathrm{SLIC}}$, $\rho = 1e-3$, and $\lambda_{\mathrm{TV}} = 1e-3$ for SUSRLR-TV, $\mathrm{iteration} = 20000$ for SUnCNN, and $\lambda = 1e-9$ and $\tau = 1e-4$ for SBWCRLRU.

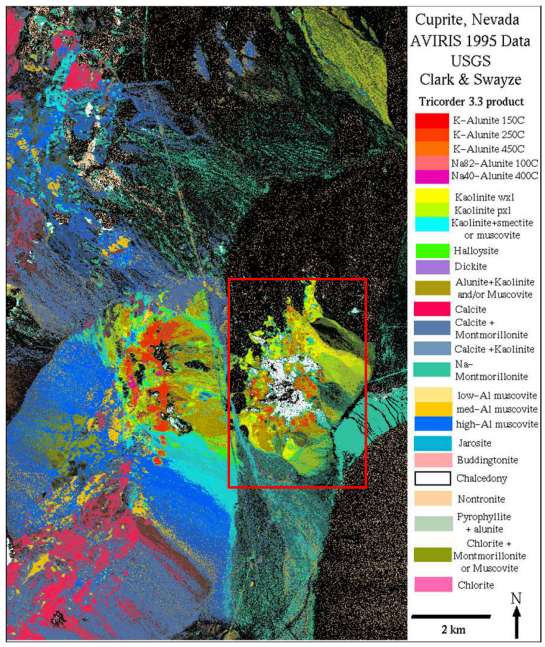

Fig. 6. USGS map showing the distribution of different minerals in Cuprite mining district in Nevada.

TABLE III
SRE AND RMSE VALUES OF DIFFERENT UNMIXING ALGORITHMS

Data	Criteria	**SUnSAL-TV**	**S^{2}WSU**	**MUA$_{SLIC}$**	**SUSRLR-TV**	**SUnCNN**	**SBWCRLRU**
Samson	SRE	16.87	15.55	16.18	15.52	12.74	**17.03**
	RMSE	0.0719	0.0837	0.0778	0.0840	0.1158	**0.0706**
		$\lambda = 5e-3$ $\lambda_{TV} = 7e-3$	$\lambda = 10e-3$	$\lambda_1 = 7e-3$ $\lambda_2 = 7e-2$	$\rho = 5e-2$ $\lambda_{TV} = 1e-2$	$Iter = 20000$	$\tau = 1e-2$ $\lambda = 1e-2$
Jasper	SRE	16.72	15.10	**18.10**	16.93	16.66	17.37
	RMSE	0.0627	0.0756	**0.0535**	0.0612	0.0613	0.0582
		$\lambda = 5e-3$ $\lambda_{TV} = 7e-3$	$\lambda = 10e-3$	$\lambda_1 = 1e-3$ $\lambda_2 = 1e-2$	$\rho = 1e-1$ $\lambda_{TV} = 1e-2$	$Iter = 20000$	$\tau = 1e-3$ $\lambda = 1e-4$

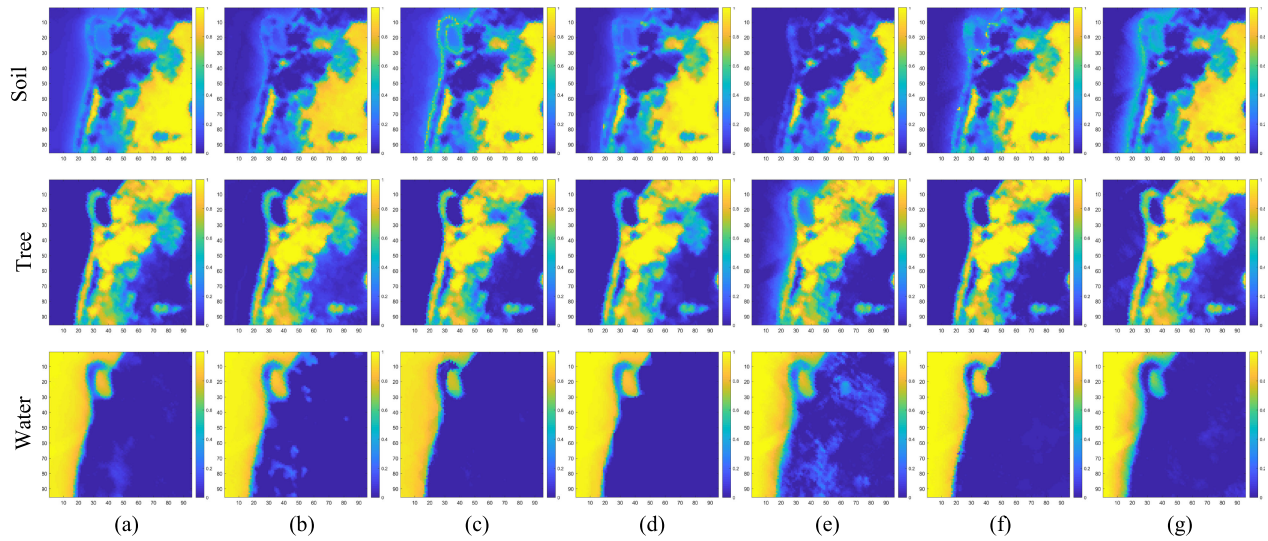

Fig. 7. Abundance maps estimated of the Samson dataset. (a) SUnSAL-TV. (b) S^{2}WSU. (c) MUA$_{\mathrm{SLIC}}$. (d) SUSRLR-TV. (e) SUnCNN. (f) SBWCRLRU. (g) Ground truth.

TABLE IV
COMPUTATION TIMES OF DIFFERENT UNMIXING ALGORITHMS (IN MIN)

Data	Criteria	**SUnSAL-TV**	**S^{2}WSU**	**MUA$_{SLIC}$**	**SUSRLR-TV**	**SUnCNN**	**SBWCRLRU**
Cuprite	TIME	41.28	16.34	**2.31**	60.18	159.58	19.81

The quantitative evaluation of the Samson and Jasper Ridge datasets is provided in Table III. Affected by the complex conditions of the real scene, the average of SRE and RMSE values between the estimated abundance maps and the ground-truth maps are compared to qualitatively evaluate the unmixing performance. It can be seen that most of the algorithms can perform well. Among them, the SBWCRLRU method is significantly better than SUnCNN with sparsity constraints in Samson datasets.

Visual comparisons of the estimated abundance maps by all approaches are presented in Figs. 7–9. It can be seen that the proposed method provides basically the same visual effect as the ground truth abundance maps, which is consistent with the quantitative evaluation, while other methods produce incorrect abundance estimated maps in some cases. For example, the SUnCNN cannot completely distinguish water and soil in Samson data, and S^{2}WSU has some problems in distinguishing water and road in Jasper Ridge data.

Since the ground truth abundance maps of the Cuprite dataset are unavailable, the computation times of all methods are presented in Table IV. The computation times of the SBWCRLRU is considerable as compared to other methods except the MUA$_{\mathrm{SLIC}}$ algorithm. From all the real data experiments results, it can be concluded that the proposed approach SBWCRLRU exhibits better unmixing capabilities for real complex hyperspectral images, and is a valid unmixing algorithm for hyperspectral unmixing.

V. DISCUSSIONS

To further study the effectiveness of the proposed SBWCRLRU algorithm, we mainly focus on the regularization

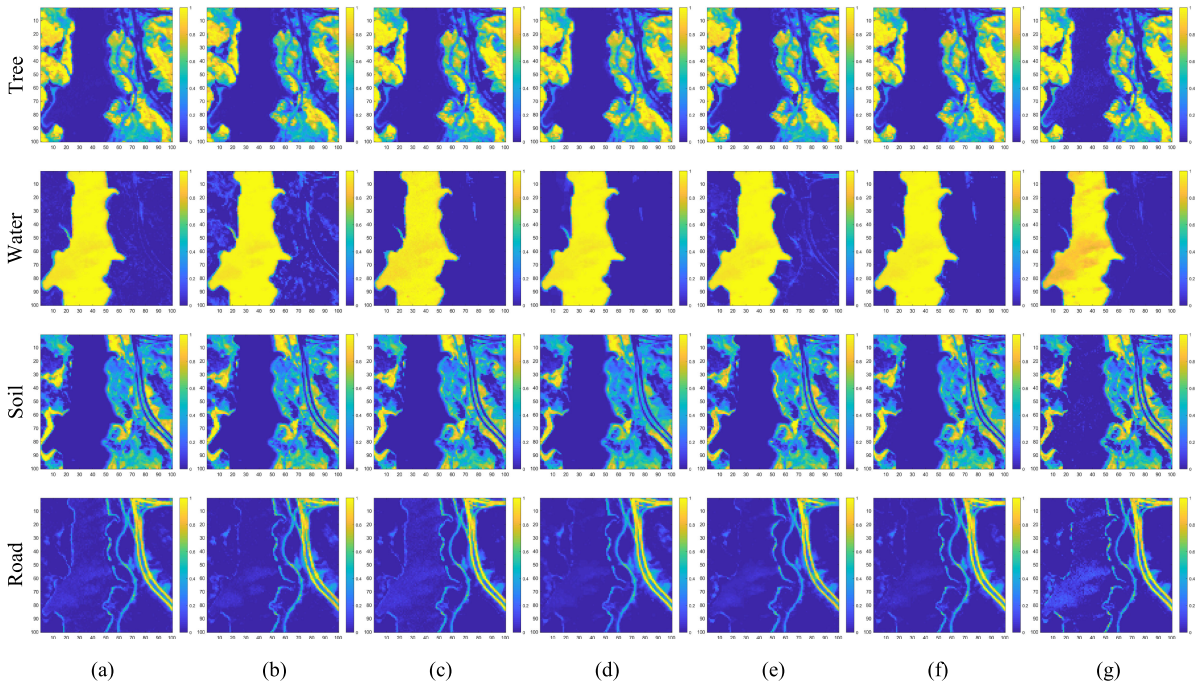

Fig. 8. Abundance maps estimated of the Jasper Ridge dataset. (a) SUnSAL-TV. (b) S^2WSU. (c) $\mathrm{MUA}_{\mathrm{SLIC}}$. (d) SUSRLR-TV. (e) SUnCNN. (f) SBWCRLRU. (g) Ground truth.

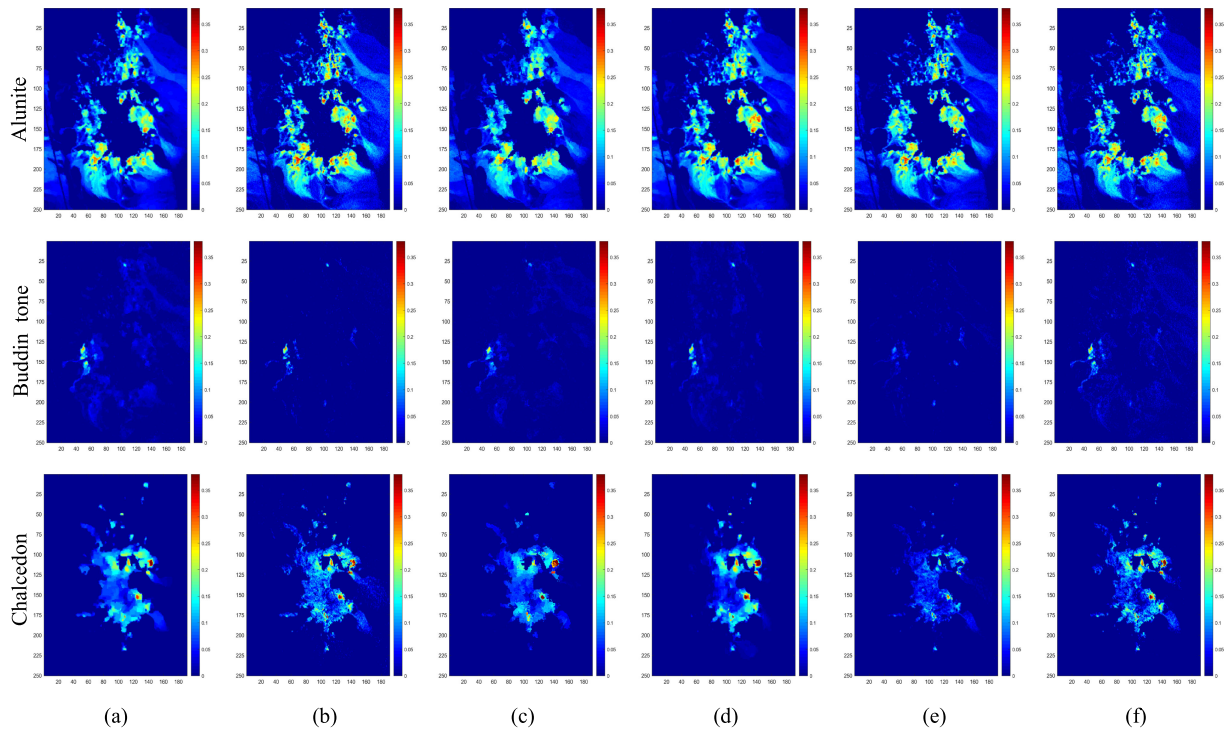

Fig. 9. Abundance maps estimated of the Cuprite dataset. (a) SUnSAL-TV. (b) S^2WSU. (c) $\mathrm{MUA}_{\mathrm{SLIC}}$. (d) SUSRLR-TV. (e) SUnCNN. (f) SBWCRLRU.

parameter τ and λ, the penalty parameter μ, the effectiveness of the reweighting strategy, the number of superpixels, and the convergence of algorithm are analyzed on the simulated data.

1) *Parameter sensitivity analysis:* For simplicity, the simulated hyperspectral datasets SD1 and SD2 under different SNR levels are used to analyze the influence of parameters. The objective function contains regularization parameters τ and λ, and the penalty parameter μ in the proposed SBWCRLRU algorithm. Here, the change of parameter λ indicates the effect of collaborative sparsity on unmixing,

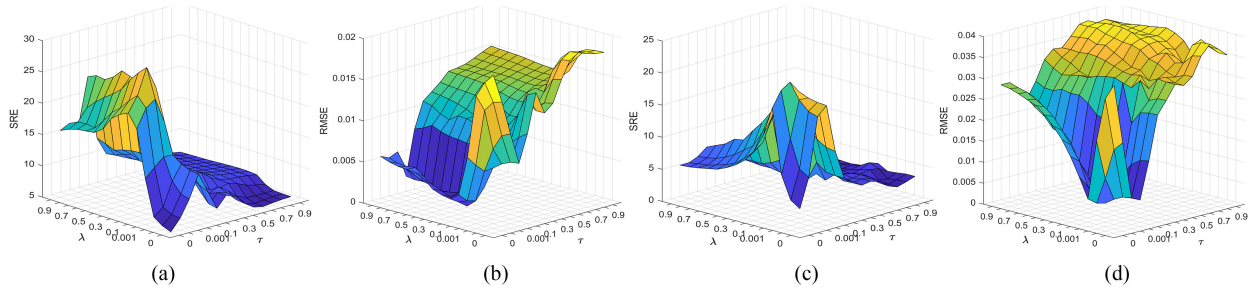

Fig. 10. SRE or RMSE as function of parameter λ and τ (SNR $=$ 30 dB). (a) SRE of SD1. (b) RMSE of SD1. (c) SRE of SD2. (d) RMSE of SD2.

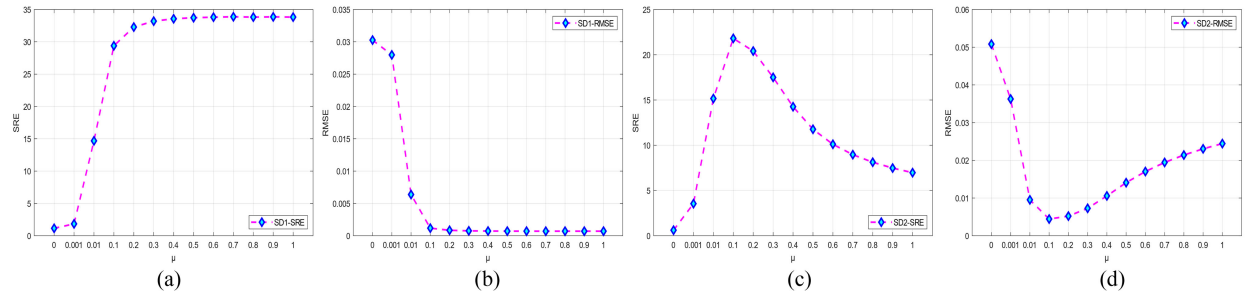

Fig. 11. SRE or RMSE as function of μ (SNR $=$ 30 dB). (a) SRE of SD1. (b) RMSE of SD1. (c) SRE of SD2. (d) RMSE of SD2.

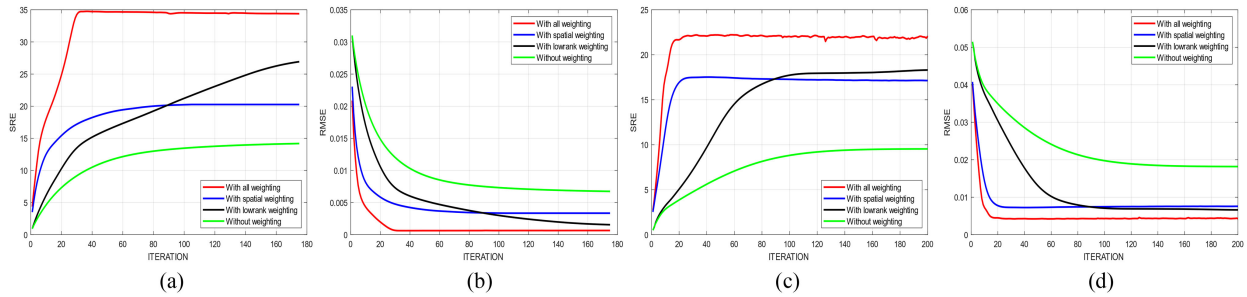

Fig. 12. Performance of SBWCRLRU obtained by different reweighting strategy. (a) SRE of SD1. (b) RMSE of SD1. (c) SRE of SD2. (d) RMSE of SD2.

and the change of parameter τ states the influence of reweighted low-rank on unmixing. After the initialization is obtained, the penalty parameter μ is first set to 0.1, and then we select τ and λ from the set of {0, 0.0001, 0.001, 0.01, 0.1, 0.2, 0.3, 0.4, 0.5, 0.6, 0.7, 0.8, 0.9, 1}. The unmixing results of the terms SRE and RMSE, as a function of the parameters τ and λ, are presented in Fig. 10, it can be clearly observed that the unmixing results of SBWCRLRU are stable as τ and λ change in the range of 0.1∼0.5 and 0.0001∼0.001 for SD1, and 0.001∼0.01 and 0.0001∼0.001 for SD2. Therefore, comprehensively consider the change of SRE and RMSE, $\tau = 0.2$ and $\lambda = 0.001$ to SD1 and $\tau = 0.01$ and $\lambda = 0.0001$ to SD2 are further used for our proposed unmixing model in the simulated datasets with 30 dB.

2) To analyze the influence of the penalty parameter, the regularization parameters τ and λ are fixed, and the transformation range of parameter μ is the same as τ and λ. The SRE and RMSE as a function of the penalty parameter μ are presented in Fig. 11. It can be seen that SRE reaches the maximum value and RMSE is the minimum value when μ is 0.9 for SD1, and 0.1 for SD2. As a consequence, the optimal μ is set in the following simulation experiments.
3) *Effectiveness of the weighting strategy:* The influence of the weighting strategy on the unmixing effect is shown in Fig. 12. It can be concluded that without weighting and with a single weighting strategy the unmixing effect is worse than with sparse and low-rank weighting together. Moreover, the SBWCRLRU algorithm with both weights produces an overall robust convergence and stability behavior.
4) *Number of superpixels*: The influence of the number of superpixels on the sparse unmixing accuracy under the different SNR levels is discussed. The simulation test is carried out with SD1 and SD2 by selecting the cluster size among the target integer values $\sqrt{N/K} \in \{2, \ldots, 15\}$. The SRE (dB), and RMSE by SBWCRLRU algorithm

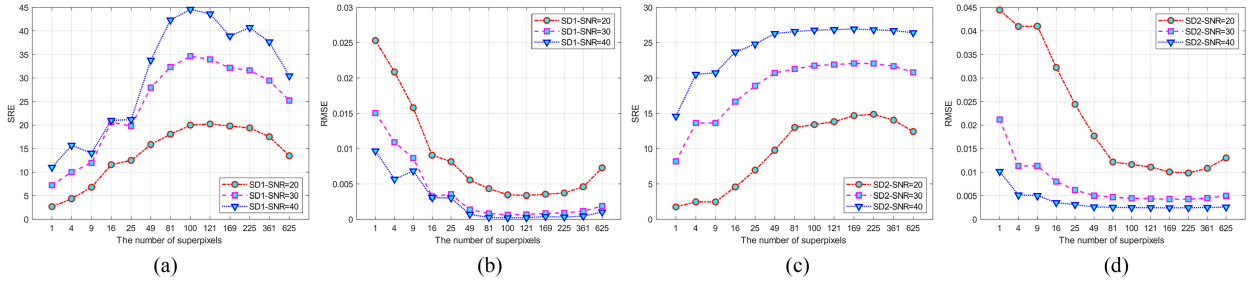

Fig. 13. Performance of SBWCRLRU obtained by different superpixel segmentation blocks. (a) SRE of SD1. (b) RMSE of SD1. (c) SRE of SD2. (d) RMSE of SD2.

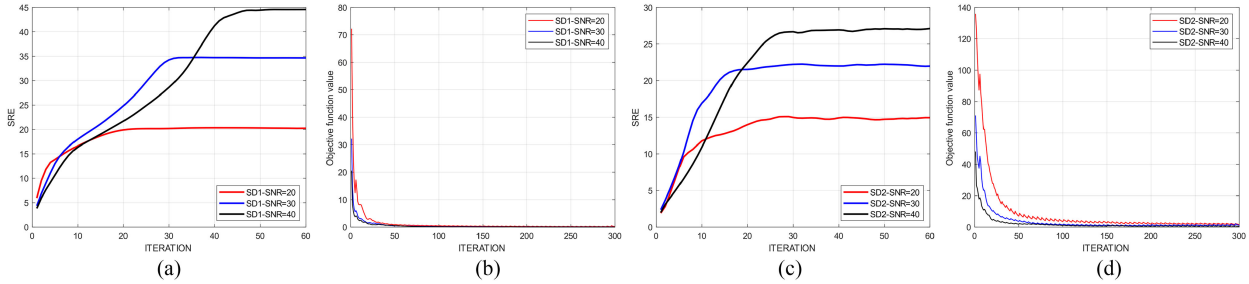

Fig. 14. Convergence curves of SBWCRLRU obtained by different SNR levels. (a) SRE of SD1. (b) Residuals of SD1. (c) SRE of SD2. (d) Residuals of SD2.

with different value of number superpixels are presented in Fig. 13. It can be observed that while the count of superpixels increases, the SRE value first increases (RMSE value decreases), but when a certain number is reached, the SRE achieves the maximum value (the RMSE value is minimum). Obviously, selecting the appropriate number of superpixels is an inevitable requirement for unmixing in SBWCRLRU. In the simulation experiments, each superpixel is composed of a certain number of pixels, and satisfactory results can be obtained in the range of 50 to 300.

5) *Convergence analysis:* Here, the objective function values in each inner loop iteration and SRE values in each outer loop iteration over simulated data at all SNR levels are recorded. The convergence curves are described in Fig. 14. As shown in Fig. 14(b) and (d), all the objective function values decrease monotonically with the increase of the number of iterations, which verifies the convergence of the SBWCRLRU. Fig. 14(a) and (c) show that the relative error between restored abundance X and the truth abundance X_{ture} becomes smaller when the number of iterations increases, and after 60 outer iterations, SBWCRLRU is able to obtain a stable solution, which indicates the stability of our method.

VI. Conclusion

In this article, the SBWCRLRU was proposed for hyperspectral image analysis. Superpixel-based method promoted adjacent pixels to have similar constituent endmembers and corresponding fractional abundance. Moreover, weighted collaborative sparse regression and reweighted LRR strategy were utilized to fully enhance the abundance sparse and spatial consistency. The experiments on both simulated and real data illustrated that the proposed algorithm SBWCRLRU efficiently improved the performance of hyperspectral unmixing and overcame the problem of edge blur caused by the TV regularization. More important, the proposed method showed improved results in visual quality and quantitative comparison. The related future research lies on exploitation of a more efficient optimization algorithm to circumvent the computational complexity.

Appendix

The optimization problem of the proposed SBWCRLRU algorithm can be written as

$$\arg\min_{X} \frac{1}{2}\|DX - Y\|_F^2 + \lambda \sum_{k=1}^{S} \|X_k\|_{a,2,1} + \tau \sum_{k=1}^{S}\sum_{j=1}^{R} \|X_k\|_{b,*} + \ell_{R_+}(X). \tag{15}$$

Equation (15) is a nonconvex and nonsmooth optimization problem, and the ADMM is introduced to settle this problem. First, it is necessary to divide Y into S superpixels as required, and introduce variable P as auxiliary. Then, (15) is equivalently rewritten by some substitutions, given by

$$\arg\min_{Q,P} \frac{1}{2}\|P_1 - Y\|_F^2 + \lambda \sum_{k=1}^{S} \|P_{2,k}\|_{a,2,1}$$

$$+\tau\sum_{k=1}^{S}\sum_{j=1}^{R}\|P_{3,k}\|_{b,*}+\ell_{R_+}(P_4)$$

$$\text{subject to: } P_1=DQ, P_2=Q, P_3=Q, P_4=Q \tag{16}$$

where, $\lambda\sum_{k=1}^{S}\|P_{2,k}\|_{a,2,1}$ accounts for the weighted collaborative sparse regression in data for each superpixel, $\tau\sum_{k=1}^{S}\sum_{j=1}^{R}\|P_{3,k}\|_{b,*}$ calculates the submatrices reweighted nuclear norm for each superpixel, to make notations more concisely, given by

$$P=\begin{bmatrix}P_1\\P_2\\P_3\\P_4\end{bmatrix}, G=\begin{bmatrix}D\\I\\I\\I\end{bmatrix}, B=\begin{bmatrix}-I&0&0&0\\0&-I&0&0\\0&0&-I&0\\0&0&0&-I\end{bmatrix}$$

and

$$g(P,Q)=\tfrac{1}{2}\|P_1-Y\|_F^2+\lambda\sum_{k=1}^{S}\|P_{2,k}\|_{a,2,1}+\tau\sum_{k=1}^{S}\sum_{j=1}^{R}\|P_{3,k}\|_{b,*}+\ell_{R_+}(P_4).$$

Then, the optimization problem (16) can be further expressed in a compact form

$$\min_{Q,P} g(P,Q)\ \text{s.t.}GQ+BP=0$$

To cope with the abovementioned model by the ADMM framework, and the optimization of (16) is converted to settle the following augmented Lagrangian function

$$\mathcal{L}_\mu(Q,P,M)=g(P,Q)+\frac{\mu}{2}\|GQ+BP-M\|_F^2 \tag{17}$$

where, $\mu>0$ is a penalty parameter, and $M=[M_1,M_2,M_3,M_4]^T$ denotes the augmented Lagrange multipliers. Then, the ADMM frameworks are derived as

$$\begin{aligned}Q^{(t+1)}&=\arg\min_{Q}\mathcal{L}_\mu(Q,P^{(t)},M^{(t)})\\P^{(t+1)}&=\arg\min_{P}\mathcal{L}_\mu(Q^{(t)},P,M^{(t)})\\M^{(t+1)}&=M^{(t)}-(GQ^{(t+1)}+BP^{(t+1)}).\end{aligned} \tag{18}$$

The typical approach adopted to tackle this issue is to optimize the function on one variable iteratively. The detail for each subproblem of (18) is presented as follows. First, after removing the constant terms, the Q subproblem is equivalent to settle

$$Q^{(t+1)}=\arg\min_{Q}\frac{\mu}{2}\left\|DQ-P_1^{(t)}-M_1^{(t)}\right\|_F^2+\sum_{i=2,3,4}\frac{\mu}{2}\left\|Q-P_i^{(t)}-M_i^{(t)}\right\|_F^2. \tag{19}$$

It is a least-squares problem. The solution to (19) by taking the partial derivative is simply as

$$Q^{(t+1)}=(D^TD+3I)^{-1}(D^T(P_1^{(t)}+M_1^{(t)})+P_2^{(t)}+M_2^{(t)}+P_3^{(t)}+M_3^{(t)}+P_4^{(t)}+M_4^{(t)}) \tag{20}$$

where I is the identity matrix, D^T represents the transpose of D. Then, the P subproblem is decoupled into four parts and each part has a closed-form solution. To compute P_1, the optimization problem is performed as

$$P_1^{(t+1)}=\arg\min_{P_1}\frac{1}{2}\|P_1-Y\|_F^2+\frac{\mu}{2}\left\|DQ^{(t+1)}-P_1-M_1^{(t)}\right\|_F^2. \tag{21}$$

A simple calculation gives

$$P_1^{(t+1)}=\frac{1}{1+\mu}\left(Y+\mu(DQ^{(t+1)}-M_1^{(t)})\right). \tag{22}$$

Then, P_2 is computed by solving the following optimization problem:

$$P_2^{(t+1)}=\arg\min_{P_2}\lambda\sum_{k=1}^{S}\|P_{2,k}\|_{a,2,1}+\frac{\mu}{2}\left\|Q^{(t+1)}-P_2-M_2^{(t)}\right\|_F^2. \tag{23}$$

By dividing the abundance matrix X into a predefined number of superpixel blocks, it then can be acquired $Q^{(t+1)}=[Q_1^{(t+1)},\ldots,Q_S^{(t+1)}]$ and $P_2=[P_{2,1},\ldots,P_{2,S}]$, and the corresponding segmentation $M_2^{(t)}=[M_{2,1}^{(t)},\ldots,M_{2,S}^{(t)}]$. Since collaborative sparsity regularization of object function (23) is proper, strictly convex subproblem, P_2 reduces to the well-known *vect_soft threshold* [20], [58], and the solution is obtained as

$$\begin{aligned}&\min_{P_{2,k}}\lambda\|P_{2,k}\|_{a,2,1}+\frac{\mu}{2}\left\|Q_k^{(t+1)}-P_{2,k}-M_{2,k}^{(t)}\right\|_F^2\\&(P_{2,k}^{(t+1)})^{[i]}=vect\_soft_{\frac{\lambda}{\mu}a}\left((Q_k^{(t+1)}-M_{2,k}^{(t)})^{[i]}\right).\end{aligned} \tag{24}$$

For $k=1,\ldots,S,\ i=1,\ldots,m,\ vect\_soft_\alpha(\cdot)$ is defined by

$$\text{vect\_soft}_\alpha(x)=x\frac{\max\{\|x\|_2-\alpha,0\}}{\max\{\|x\|_2-\alpha,0\}+\alpha}. \tag{25}$$

Next, for the P_3 subproblem, it is equivalent to solve the following minimization problem:

$$P_3^{(t+1)}=\arg\min_{P_3}\tau\sum_{k=1}^{S}\sum_{j=1}^{R}\|P_{3,k}\|_{b,*}+\frac{\mu}{2}\left\|Q^{(t+1)}-P_3-M_3^{(t)}\right\|_F^2. \tag{26}$$

Before solving the P_3 subproblem, abundance matrix X is also divided into the predefined number of superpixel blocks, and performed on the submatrices in each superpixel to enhance the unmixing, where $j=1,\ldots,R,$ and R is the number of submatrices in each superpixel.

Let the singular value decomposition (SVD) of abundance matrix X be $UDiag((\sigma_1)_+,\ldots,(\sigma_r)_+)V^T$, here, $r=rank(X)$, $(x)_+=\max\{x,0\}$, U and V are the unitary matrices corresponding to the SVD of X, and σ_i denote the i

th singular value of X, $i = 1, \ldots, r$. Then, the SVT [39], [40] operator are as follows:

$$\mathcal{T}_{b,\tau}(X) = U\mathrm{Diag}\left((\sigma_1 - \tau b_1)_+, \ldots, (\sigma_r - \tau b_r)_+\right) V^T. \tag{27}$$

Then, the solution to P_3 is explicitly given by

$$P_{3,k}^{(t+1)} = \mathcal{T}_{b,\frac{\tau}{\mu}}(Q_k^{(t+1)} - M_{3,k}^{(t)}). \tag{28}$$

The subproblem with respect to P_4 gives

$$P_4^{(t+1)} = \arg\min_{P_4} \ell_{R_+}(P_4) + \frac{\mu}{2}\left\|Q^{(t+1)} - P_4 - M_4^{(t)}\right\|_F^2. \tag{29}$$

The role of the $\ell_{R_+}(P_4)$ term is an indicator function of the positive vector space. And the solution to P_4 is given by

$$P_4^{(t+1)} = \max(Q^{(t+1)} - M_4^{(t)}, 0). \tag{30}$$

Finally, the multipliers M are sequentially updated as

$$\begin{aligned} M_1^{(t+1)} &= M_1^{(t)} - DQ^{(t+1)} + M_1^{(t+1)} \\ M_i^{(t+1)} &= M_i^{(t)} - Q^{(t+1)} + M_i^{(t+1)}, i = 2, 3, 4. \end{aligned} \tag{31}$$

ACKNOWLEDGMENT

The authors would like to thank Prof. R. A. Borsoi for sharing the multiscale spatial regularization unmixing algorithm (MUA) code, Prof. B. Rasti for sharing a sparse unmixing technique using a convolutional neural network (SUnCNN) code, and Prof. Ruyi Feng for sharing sparse unmixing by superpixel-based reweighted low-rank and total variation (SUSRLR-TV) code.

REFERENCES

[1] H. Su, Y. Yu, Q. Du, and P. Du, "Ensemble learning for hyperspectral image classification using tangent collaborative representation," *IEEE Trans. Geosci. Remote Sens.*, vol. 58, no. 6, pp. 3778–3790, Jun. 2020.

[2] H. Su, Z. Wu, A.-X. Zhu, and Q. Du, "Low rank and collaborative representation for hyperspectral anomaly detection via robust dictionary construction," *ISPRS J. Photogramm. Remote Sens.*, vol. 169, pp. 195–211, Nov. 2020.

[3] H. Su, W. Yao, Z. Wu, P. Zheng, and Q. Du, "Kernel low-rank representation with elastic net for China coastal wetland land cover classification using GF-5 hyperspectral imagery," *ISPRS J. Photogramm. Remote Sens.*, vol. 171, pp. 238–252, Jan. 2021.

[4] D. Hong *et al.*, "Interpretable hyperspectral artificial intelligence: When nonconvex modeling meets hyperspectral remote sensing," *IEEE Geosci. Remote Sens. Mag.*, vol. 9, no. 2, pp. 52–87, Jun. 2021.

[5] J. M. Bioucas-Dias *et al.*, "Hyperspectral unmixing overview: Geometrical, statistical, and sparse regression-based approaches," *IEEE J. Sel. Top. Appl. Earth Obs. Remote Sens.*, vol. 5, no. 2, pp. 354–379, Apr. 2012.

[6] N. Keshava and J. F. Mustard, "Spectral unmixing," *IEEE Signal Process. Mag.*, vol. 19, no. 1, pp. 44–57, Jan. 2002.

[7] M. E. Winter, "N-FINDR: An algorithm for fast autonomous spectral endmember determination in hyperspectral data," in *Proc. Int. Geosci. Remote Sens. Symp. (IGARSS)*, Oct. 1999, pp. 266–275.

[8] J. M. P. Nascimento and J. M. B. Dias, "Vertex component analysis: A fast algorithm to unmix hyperspectral data," *IEEE Trans. Geosci. Remote Sens.*, vol. 43, no. 4, pp. 898–910, Apr. 2005.

[9] G. Lü, M. Batty, J. Strobl, H. Lin, A.-X. Zhu, and M. Chen, "Reflections and speculations on the progress in geographic information systems (GIS): A geographic perspective," *Int. J. Geogr. Inf. Sci.*, vol. 33, no. 2, pp. 346–367, Feb. 2019.

[10] J. M. P. Nascimento and J. M. B. Dias, "Does independent component analysis play a role in unmixing hyperspectral data," *IEEE Trans. Geosci. Remote Sens.*, vol. 43, no. 1, pp. 175–187, Jan. 2005.

[11] N. Dobigeon, S. Moussaoui, M. Coulon, J.-Y. Tourneret, and A. O. Hero, "Joint Bayesian endmember extraction and linear unmixing for hyperspectral imagery," *IEEE Trans. Signal Process.*, vol. 57, no. 11, pp. 4355–4368, Nov. 2009.

[12] L. Miao and H. Qi, "Endmember extraction from highly mixed data using minimum volume constrained nonnegative matrix factorization," *IEEE Trans. Geosci. Remote Sens.*, vol. 45, no. 3, pp. 765–777, Mar. 2007.

[13] J. Peng, Y. Zhou, W. Sun, Q. Du, and L. Xia, "Self-Paced nonnegative matrix factorization for hyperspectral unmixing," *IEEE Trans. Geosci. Remote Sens.*, vol. 59, no. 2, pp. 1501–1515, Feb. 2021.

[14] P. Zheng, H. Su, and Q. Du, "Sparse and low-rank constrained tensor factorization for hyperspectral image unmixing," *IEEE J. Sel. Top. Appl. Earth Obs. Remote Sens.*, vol. 14, pp. 1754–1767, Jan. 2021.

[15] M.-D. Iordache, J. M. Bioucas-Dias, and A. Plaza, "Sparse unmixing of hyperspectral data," *IEEE Trans. Geosci. Remote Sens.*, vol. 49, no. 6, pp. 2014–2039, Jun. 2011.

[16] D. Hong, N. Yokoya, J. Chanussot, and X. X. Zhu, "An augmented linear mixing model to address spectral variability for hyperspectral unmixing," *IEEE Trans. Image Process.*, vol. 28, no. 4, pp. 1923–1938, Apr. 2019.

[17] C. Li, T. Sun, K. F. Kelly, and Y. Zhang, "A compressive sensing and unmixing scheme for hyperspectral data processing," *IEEE Trans. Image Process.*, vol. 21, no. 3, pp. 1200–1210, Mar. 2012.

[18] L. Wang, Y. Feng, Y. Gao, Z. Wang, and M. He, "Compressed sensing reconstruction of hyperspectral images based on spectral unmixing," *IEEE J. Sel. Top. Appl. Earth Obs. Remote Sens.*, vol. 11, no. 4, pp. 1266–1284, Apr. 2018.

[19] J. M. Bioucas-Dias and M. A. T. Figueiredo, "Alternating direction algorithms for constrained sparse regression: Application to hyperspectral unmixing," in *Proc. 2nd Workshop Hyperspectral Image Signal Process., Evol. Remote Sens.*, Jun. 2010, pp. 1–4.

[20] M. Iordache, J. M. Bioucas-Dias, and A. Plaza, "Collaborative sparse regression for hyperspectral unmixing," *IEEE Trans. Geosci. Remote Sens.*, vol. 52, no. 1, pp. 341–354, Jan. 2014.

[21] S. Zhang, J. Li, K. Liu, C. Deng, L. Liu, and A. Plaza, "Hyperspectral unmixing based on local collaborative sparse regression," *IEEE Geosci. Remote Sens. Lett.*, vol. 13, no. 5, pp. 631–635, May 2016.

[22] R. Wang, H.-C. Li, A. Pizurica, J. Li, A. Plaza, and W. J. Emery, "Hyperspectral unmixing using double reweighted sparse regression and total variation," *IEEE Geosci. Remote Sens. Lett.*, vol. 14, no. 7, pp. 1146–1150, Jul. 2017.

[23] S. Zhang, J. Li, H.-C. Li, C. Deng, and A. Plaza, "Spectral–Spatial weighted sparse regression for hyperspectral image unmixing," *IEEE Trans. Geosci. Remote Sens.*, vol. 56, no. 6, pp. 3265–3276, Jun. 2018.

[24] M. Iordache, J. M. Bioucas-Dias, and A. Plaza, "Total variation spatial regularization for sparse hyperspectral unmixing," *IEEE Trans. Geosci. Remote Sens.*, vol. 50, no. 11, pp. 4484–4502, Nov. 2012.

[25] J. Yao, D. Meng, Q. Zhao, W. Cao, and Z. Xu, "Nonconvex-Sparsity and nonlocal-smoothness-based blind hyperspectral unmixing," *IEEE Trans. Image Process.*, vol. 28, no. 6, pp. 2991–3006, Jun. 2019.

[26] H. Wu *et al.*, "Examining the sensitivity of spatial scale in cellular automata markov chain simulation of land use change," *Int. J. Geogr. Inf. Sci.*, vol. 33, no. 5, pp. 1040–1061, May 2019.

[27] H. Koo *et al.*, "Position paper: Sensitivity analysis of spatially distributed environmental models- a pragmatic framework for the exploration of uncertainty sources," *Environ. Model. Softw.*, vol. 134, Dec. 2020, Art. no. 104857.

[28] G. Lü, C. Zhou, H. Lin, M. Chen, S. Yue, and Y. Wen, "Development overview and some thoughts ongeographic synthesis," *Chin. Sci. Bull.*, vol. 66, no. 20, pp. 2542–2554, Jul. 2021.

[29] S. Subudhi, R. N. Patro, P. K. Biswal, and F. Dell'Acqua, "A survey on superpixel segmentation as a preprocessing step in hyperspectral image analysis," *IEEE J. Sel. Top. Appl. Earth Obs. Remote Sens.*, vol. 14, pp. 5015–5035, Apr. 2021.

[30] R. A. Borsoi, T. Imbiriba, J. C. M. Bermudez, and C. Richard, "A fast multiscale spatial regularization for sparse hyperspectral unmixing," *IEEE Geosci. Remote Sens. Lett.*, vol. 16, no. 4, pp. 598–602, Apr. 2019.

[31] L. Yang, J. Peng, H. Su, L. Xu, Y. Wang, and B. Yu, "Combined nonlocal spatial information and spatial group sparsity in NMF for hyperspectral unmixing," *IEEE Geosci. Remote Sens. Lett.*, vol. 17, no. 10, pp. 1767–1771, Oct. 2020.

[32] S. Zhang *et al.*, "Superpixel-guided sparse unmixing for remotely sensed hyperspectral imagery," in *Proc. IEEE Int. Geosci. Remote Sens. Symp.*, 2019, pp. 2155–2158.

[33] Z. Li, J. Chen, and S. Rahardja, "Superpixel construction for hyperspectral unmixing," in *Proc. 26th Eur. Signal Process. Conf.*, 2018, pp. 647–651.

[34] T. Ince, "Superpixel-based graph Laplacian regularization for sparse hyperspectral unmixing," *IEEE Geosci. Remote Sens. Lett.*, pp. 1–5, doi: 10.1109/LGRS.2020.3027055.
[35] T. Ince, "Double spatial graph laplacian regularization for sparse unmixing," *IEEE Geosci. Remote Sens. Lett.*, pp. 1–5, doi: 10.1109/LGRS.2021.3065989.
[36] D. Hong, N. Yokoya, J. Chanussot, J. Xu, and X. X. Zhu, "Joint and progressive subspace analysis (JPSA) with spatial–spectral manifold alignment for semisupervised hyperspectral dimensionality reduction," *IEEE Trans. Cybern.*, vol. 51, no. 7, pp. 3602–3615, Jul. 2021.
[37] L. Gao, D. Hong, J. Yao, B. Zhang, P. Gamba, and J. Chanussot, "Spectral superresolution of multispectral imagery with joint sparse and low-rank learning," *IEEE Trans. Geosci. Remote Sens.*, vol. 59, no. 3, pp. 2269–2280, Mar. 2021.
[38] P. V. Giampouras, K. E. Themelis, A. A. Rontogiannis, and K. D. Koutroumbas, "Simultaneously sparse and low-rank abundance matrix estimation for hyperspectral image unmixing," *IEEE Trans. Geosci. Remote Sens.*, vol. 54, no. 8, pp. 4775–4789, Aug. 2016.
[39] J. Huang, T. Huang, L. Deng, and X. Zhao, "Joint-sparse-blocks and low-rank representation for hyperspectral unmixing," *IEEE Trans. Geosci. Remote Sens.*, vol. 57, no. 4, pp. 2419–2438, Apr. 2019.
[40] H. Li, R. Feng, L. Wang, Y. Zhong, and L. Zhang, "Superpixel-based reweighted low-rank and total variation sparse unmixing for hyperspectral remote sensing imagery," *IEEE Trans. Geosci. Remote Sens.*, vol. 59, no. 1, pp. 629–647, Jan. 2021.
[41] E. J. Candes and T. Tao, "Decoding by linear programming," *IEEE Trans. Inf. Theory*, vol. 51, no. 12, pp. 4203–4215, Dec. 2005.
[42] E. J. Candes and T. Tao, "Near-optimal signal recovery from random projections: Universal encoding strategies," *IEEE Trans. Inf. Theory*, vol. 52, no. 12, pp. 5406–5425, Dec. 2006.
[43] S. S. Chen, D. L. Donoho, and M. A. Saunders, "Atomic decomposition by basis pursuit," *SIAM Rev.*, vol. 43, no. 1, pp. 129–159, Jan. 2001.
[44] E. J. Candès, J. K. Romberg, and T. Tao, "Stable signal recovery from incomplete and inaccurate measurements," *Commun. Pure Appl. Math.*, vol. 59, no. 8, pp. 1207–1223, Aug. 2006.
[45] H. Sun and A. Zare, "Map-guided hyperspectral image superpixel segmentation using proportion maps," in *Proc. IEEE Int. Geosci. Remote Sens. Symp.*, 2017, pp. 3751–3754.
[46] R. Achanta, A. Shaji, K. Smith, A. Lucchi, P. Fua, and S. Süsstrunk, "SLIC superpixels compared to state-of-the-art superpixel methods," *IEEE Trans. Pattern Anal. Mach. Intell.*, vol. 34, no. 11, pp. 2274–2282, Nov. 2012.
[47] H. Wu, A. Lin, K. C. Clarke, W. Shi, A. Cardenas-Tristan, and Z. Tu, "A comprehensive quality assessment framework for linear features from volunteered geographic information," *Int. J. Geogr. Inf. Sci.*, vol. 35, no. 9, pp. 1826–1847, Sep. 2021.
[48] M. Q. Alkhatib and M. Velez-Reyes, "Improved spatial-spectral superpixel hyperspectral unmixing," *Remote Sens.*, vol. 11, no. 20, Oct. 2019, Art. no. 2374.
[49] H. Su, Y. Yu, Z. Wu, and Q. Du, "Random subspace-based k-nearest class collaborative representation for hyperspectral image classification," *IEEE Trans. Geosci. Remote Sens.*, vol. 59, no. 8, pp. 6840–6853, Aug. 2021.
[50] L. Qi, J. Li, Y. Wang, Y. Huang, and X. Gao, "Spectral–spatial-weighted multiview collaborative sparse unmixing for hyperspectral images," *IEEE Trans. Geosci. Remote Sens.*, vol. 58, no. 12, pp. 8766–8779, Dec. 2020.
[51] H. Su, B. Zhao, Q. Du, and P. Du, "Kernel collaborative representation with local correlation features for hyperspectral image classification," *IEEE Trans. Geosci. Remote Sens.*, vol. 57, no. 2, pp. 1230–1241, Feb. 2019.
[52] Y. Peng, J. Suo, Q. Dai, and W. Xu, "Reweighted low-rank matrix recovery and its application in image restoration," *IEEE Trans. Cybern.*, vol. 44, no. 12, pp. 2418–2430, Dec. 2014.
[53] R. Wang, W. Liao, H.-C. Li, H. Zhang, and A. Pizurica, "Hyperspectral unmixing by reweighted low rank and total variation," in *Proc. 8th Workshop Hyperspectral Image Signal Process., Evol. Remote Sens.*, 2016, pp. 1–4.
[54] W. Dong, G. Shi, X. Li, Y. Ma, and F. Huang, "Compressive sensing via nonlocal low-rank regularization," *IEEE Trans. Image Process.*, vol. 23, no. 8, pp. 3618–3632, Aug. 2014.
[55] S. Gu, L. Zhang, W. Zuo, and X. Feng, "Weighted nuclear norm minimization with application to image denoising," in *Proc. IEEE Conf. Comput. Vis. Pattern Recognit.*, 2014, pp. 2862–2869.
[56] S. Boyd, N. Parikh, E. Chu, B. Peleato, and J. Eckstein, "Distributed optimization and statistical learning via the alternating direction method of multipliers," *Found. Trends Mach. Learn.*, vol. 3, no. 1, pp. 1–122, 2010.
[57] B. Rasti and B. Koirala, "SUnCNN: Sparse unmixing using unsupervised convolutional neural network," *IEEE Geosci. Remote Sens. Lett.*, pp. 1–5, doi: 10.1109/LGRS.2021.3100992.
[58] S. J. Wright, R. D. Nowak, and M. A. T. Figueiredo, "Sparse reconstruction by separable approximation," *IEEE Trans. Signal Process.*, vol. 57, no. 7, pp. 2479–2493, Jul. 2009.

Hongjun Su (Senior Member, IEEE) received the Ph.D. degree in cartography and geography information system from the Key Laboratory of Virtual Geographic Environment (Ministry of Education), Nanjing Normal University, Nanjing, China, in 2011.

He is currently a Full Professor with the School of Earth Sciences and Engineering, Hohai University, Nanjing. His research interests include hyperspectral remote sensing dimensionality reduction, classification, and spectral unmixing.

Dr. Su was the recipient of the 2016 Best Reviewer Award from the IEEE Geoscience and Remote Sensing Society. He is currently an Associate Editor for IEEE JOURNAL OF SELECTED TOPICS IN APPLIED EARTH OBSERVATIONS AND REMOTE SENSING.

Cailing Jia received the B.E. degree in surveying and mapping engineering from the School of City College, Kunming University of Science and Technology, Kunming, China, in 2019. She is currently working toward the M.E. degree in surveying and mapping from the School of Earth Sciences and Engineering, Hohai University, Nanjing, China.

Her research interests include hyperspectral remote sensing imagery, collaborative regression, low-rank representation, and machine learning in hyperspectral unmixing.

Pan Zheng received the B.E. degree in geodesy and geomatics engineering in 2018, and the M.E. degree in photogrammetry and remote sensing in 2021 from the School of Earth Sciences and Engineering, Hohai University, Nanjing, China, where she is currently working toward the Ph.D. degree in surveying and mapping.

Her research interests include hyperspectral remote sensing imagery, collaborative representation, and machine learning in hyperspectral unmixing.

Qian Du (Fellow, IEEE) received the Ph.D. degree in electrical engineering from the University of Maryland, Baltimore, MD, USA, in 2000.

She is currently the Bobby Shackouls Professor with the Department of Electrical and Computer Engineering, Mississippi State University, Starkville, MS, USA. Her research interests include hyperspectral image analysis and applications, pattern classification, data compression, and neural networks.

Prof. Du was a Co-Chair of the Data Fusion Technical Committee of the IEEE Geoscience and Remote Sensing Society from 2009 to 2013, and the Chair of the Remote Sensing and Mapping Technical Committee of the International Association for Pattern Recognition from 2010 to 2014. She was the Associate Editor for IEEE JOURNAL OF SELECTED TOPICS IN APPLIED EARTH OBSERVATIONS AND REMOTE SENSING, *Journal of Applied Remote Sensing*, and IEEE Signal Processing Letters. In 2016–2020, she was Editor-in-Chief of the IEEE JOURNAL OF SELECTED TOPICS IN APPLIED EARTH OBSERVATIONS AND REMOTE SENSING. She currently is a member of the IEEE Periodicals Review and Advisory Committee. She is a Fellow of the IEEE and SPIE-International Society for Optics and Photonics.